

GSH/pH Cascade-Responsive Nanoparticles Eliminate Methicillin-Resistant *Staphylococcus aureus* Biofilm via Synergistic Photo-Chemo Therapy

Xiaoxu Kang,[§] Xuankun Yang,[§] Fanqiang Bu, Wenli Feng, Fang Liu, Wensheng Xie, Guofeng Li,* and Xing Wang*



Cite This: <https://doi.org/10.1021/acsami.3c17198>



Read Online

ACCESS |

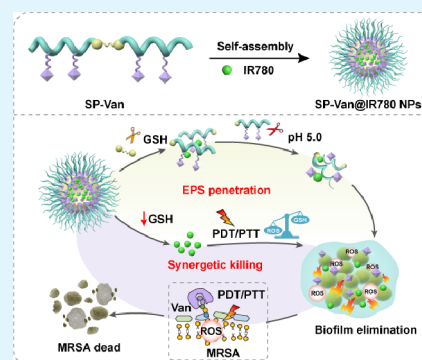
Metrics & More

Article Recommendations

Supporting Information

ABSTRACT: Bacterial biofilm infection threatens public health, and efficient treatment strategies are urgently required. Phototherapy is a potential candidate, but it is limited because of the off-targeting property, vulnerable activity, and normal tissue damage. Herein, cascade-responsive nanoparticles (NPs) with a synergistic effect of phototherapy and chemotherapy are proposed for targeted elimination of biofilms. The NPs are fabricated by encapsulating IR780 in a polycarbonate-based polymer that contains disulfide bonds in the main chain and a Schiff-base bond connecting vancomycin (Van) pendants in the side chain (denoted as SP–Van@IR780 NPs). SP–Van@IR780 NPs specifically target bacterial biofilms *in vitro* and *in vivo* by the mediation of Van pendants. Subsequently, SP–Van@IR780 NPs are decomposed into small size and achieve deep biofilm penetration due to the cleavage of disulfide bonds in the presence of GSH. Thereafter, Van is then detached from the NPs because the Schiff base bonds are broken at low pH when SP@IR780 NPs penetrate into the interior of biofilm. The released Van and IR780 exhibit a robust synergistic effect of chemotherapy and phototherapy, strongly eliminate the biofilm both *in vitro* and *in vivo*. Therefore, these biocompatible SP–Van@IR780 NPs provide a new outlook for the therapy of bacterial biofilm infection.

KEYWORDS: methicillin-resistant *Staphylococcus aureus* infection, cascade-responsive nanoparticles, mild phototherapy, chemotherapy, synergistic therapy



1. INTRODUCTION

Bacterial infection is a major medical problem that threatens public health.¹ Antibiotics are commonly used in the clinical treatment of bacterial infections.^{2–4} However, their widespread use and misuse frequently facilitates bacterial drug resistance.^{5–7} Moreover, the bacteria can further form biofilms.^{8–10} The dense extracellular polymeric substances (EPS) in biofilms exceedingly hinder the internalization of antibiotics, and greatly weaken the antibacterial efficiency regardless of using high doses of antibiotics.^{11,12} Additionally, the bacteria are willing to accumulate numerous acidic metabolites because of the hypoxia feature of biofilm.^{13,14} These metabolites give rise to the formation of a specific inner microenvironment of biofilm, in which there is a gradiently increased acid concentration from the outside to the inside.¹⁵ The hypoxic and slightly acidic environment, consequently, slows down bacterial metabolism and, thus, exacerbates bacterial tolerance to antibiotics.^{2,16,17} Therefore, there is an urgent need to develop an effective strategy to enhance the efficacy of antibiotics to achieve efficient eradication of drug-resistant bacteria and their biofilms at low doses.

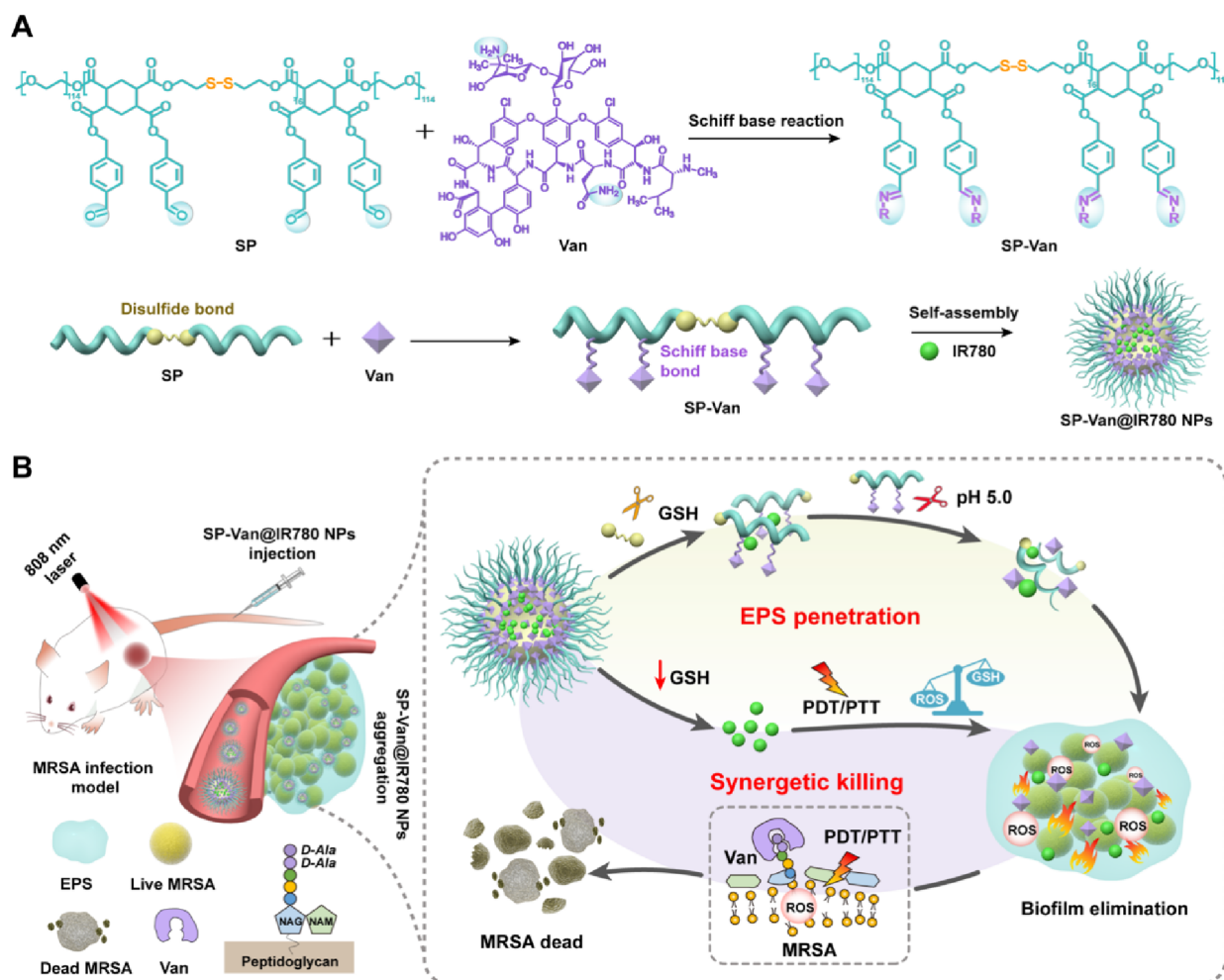
Phototherapy, including photodynamic therapy (PDT) and photothermal therapy (PTT), has been widely explored for the

treatment of bacterial infections due to its advantages of spatiotemporal selectivity, noninvasiveness, broad antibacterial spectrum, and less potency to induce antibacterial resistance.^{18–22} However, phototherapy still has some limitations. (i) The off-target of photosensitizer (PS);^{23,24} (ii) the short diffusion distance and lifetime of produced reactive oxygen species (ROS);²⁵ (iii) antioxidant enzymes and overexpressed GSH in bacterial infection microenvironment neutralize the destructive effect of PDT;^{26–29} (iv) high temperature generated by inaccurate PTT damages normal tissues.³⁰ Accordingly, the combination of phototherapy and antibiotics is a promising strategy to overcome the limitations of phototherapy, while enhancing the efficacy of antibiotics.³¹ One of the most common approaches is using nanoparticles (NPs) to precisely deliver PS and antibiotics to the site of bacterial infection thereby achieving combination treatment

Received: November 15, 2023

Revised: December 24, 2023

Accepted: December 24, 2023

Scheme 1. Schematic Illustration of the SP–Van@IR780 NPs for Killing MRSA and Its Biofilm^{a,b}

^aSynthesis and preparation of SP–Van ^bSP–Van@IR780 NPs accumulating at the MRSA infection location to kill MRSA and its biofilms by photoantibiotic synergistic therapy.

with phototherapy and antibiotics.^{32–35} In this way, phototherapy reinforces the susceptibility to antibiotic killing by interfering with bacterial metabolic activity or enhancing biofilm penetration; and complementarily, antibiotics can also boost phototherapy by promoting bacterial uptake of PS.^{31,35,36} However, the synergistic effect of drug combination is conservatism.³⁷ The effect of synergism greatly depends on the formula ratio of PS and antibiotics, which determines the performances on killing drug-resistant bacteria and biofilms.^{38,39} Moreover, the formula ratio could be altered due to the complexity of the bacterial infection microenvironment.^{40,41} This requires stable loading and on-demand release of PS and antibiotics. Therefore, novel NPs that possess stable PS and antibiotic loading in a formula ratio and precise drug release performance can amplify synergistic effects of phototherapy/antibiotic treatment against stubborn bacteria and their biofilms.

Herein, GSH/pH cascade-responsive NPs with synergistic effects of phototherapy and antibiotics were developed for the targeted eradication of methicillin-resistant *Staphylococcus aureus* (MRSA) and its biofilm (Scheme 1). First, a polycarbonate-based polymer with disulfide bonds in the main chain and pendant aldehyde groups in the side chain was synthesized, named SP. Further, vancomycin (Van) is bonded

into SP through Schiff base bonds to form SP–Van. Finally, SP–Van is used to wrap IR780 to get SP–Van@IR780 NPs. Owing to bacterial peptidoglycan targeting ability of Van, SP–Van@IR780 NPs can be actively enriched to bacterial infection sites. The overexpressed GSH in the microenvironment of bacterial infection triggers the rapid breaking of disulfide bonds, resulting in the gradual disintegration of SP–Van@IR780 NPs, which helps to achieve deep drug penetration. Meanwhile, the consumption of GSH by disulfide bonds can promote the accumulation of ROS in the infected microenvironment and sensitize the PDT effect. The IR780 and Van exhibited remarkable synergistic effects (0.28 of the fractional inhibitory concentration indices (FICI)) and significantly reduced the administered doses of IR780 and Van by 50% and 83.3%, respectively. Compared with control groups, SP–Van@IR780 NPs showed superior therapeutic effect on MRSA biofilm and mouse subcutaneous abscess. Therefore, SP–Van@IR780 NPs, utilizing a smart drug delivery system to synergize phototherapy and antibiotics, is a promising strategy for treating drug-resistant bacterial infections and their biofilms.

2. METHODS

2.1. Materials. 2,2'-dithioethanol and glutathione (GSH) were purchased from Tokyo Chemical Industry (TCI). 1,6-Hexadiol and

IR780 were purchased from Shanghai Macklin Biochemical Co., Ltd. 1,2,4,5-Cyclohexane tetracarboxylic anhydride and vancomycin (Van) were purchased from Bide Pharmatech Co., Ltd. Methoxypolyethylene glycol 5000 (mPEG₅₀₀₀-OH), 4-(hydroxymethyl) benzaldehyde, and 1,2-benzenedicarboxaldehyde (OPA) were purchased from Innochem (Beijing) Technology Co., Ltd. Dimethyl sulfoxide (DMSO), triethylamine (Et₃N), *N,N*-dimethylformamide (DMF), ethanol (EtOH), and methanol (MeOH) were purchased from J&K Scientific. Tryptone soybean broth (TSB) and tryptone soybean agar (TSA) were purchased from Sinopharm Holdings Chemical Reagents (China). Thiazolyl blue tetrazolium bromide (MTT), 1,3-diphenyliso-benzofuran (DPBF), acridineorange (AO), propidiumiodide (PI), and triton X-100 were purchased from Solarbio Science & Technology Co., Ltd. (China).

2.2. Synthesis and Characterization of Polymers and Nanoparticles.

2.2.1. Synthesis of SP-COOH and CP-COOH. 2-Hydroxyethyl disulfide (933 mg, 6.058 mmol) and 1,2,4,5-cyclohexane tetracarboxylic anhydride (1425 mg, 6.361 mmol) were placed in a round-bottled flask, and ultradry DMF (5 mL) was added as the reaction solvent. After stirring at room temperature for 24 h, mPEG₅₀₀₀-OH (3100 mg, 0.62 mmol) was added to the reaction system. Then, the reaction was carried out for another 12 h at 65 °C. At last, the mixture was purified by dialysis (Mw: 8000 Da) in deionized water for 48 h. The SP-COOH polymer was obtained after lyophilization. CP-COOH polymer can be obtained by replacing 2-hydroxyethyl disulfide with 1,6-hexadiol and following the synthesis route described above.

2.2.2. Synthesis of SP and CP. SP-COOH (500 mg, 0.03 mmol), EDC (345.1 mg, 1.8 mmol), and DMAP (219.9 mg, 1.8 mmol) were added to a round-bottled flask containing 5 mL of DMSO. The mixture was stirred at 40 °C for 4 h to activate the carboxyl groups. Then, 4-(hydroxymethyl) benzaldehyde (329.8 mg, 1.8 mmol) was added, and the mixture was collected after continuous agitation for 12 h. After dialysis, the solution was lyophilized to obtain a white solid product (SP). CP polymer was obtained by replacing SP-COOH with CP-COOH and following the synthesis route described above.

2.2.3. Synthesis of SP-Van. SP polymer (50 mg, 0.003 mmol) and vancomycin (50 mg, 0.03 mmol) were dissolved in DMSO (5 mL), and triethylamine (Et₃N, 10 μL) was added as a catalyst. The mixture was stirred at 40 °C for 24 h. After dialysis, the solution was lyophilized to obtain the product (SP-Van).

2.2.4. Preparation of NPs. SP-Van (10 mg) and IR780 (2 mg) were dissolved in a container with DMSO (1 mL). The mixed solution was stirred for 3–5 min, and then 3 mL of deionized water was slowly dripped into the mixture. After stirring was continued for 10 min, the nanoparticles were obtained. Then, the solution was placed into a dialysis bag (Mw: 3500 Da) and dialyzed with deionized water to remove DMSO and unencapsulated IR780. After 48 h of dialysis, SP-Van@IR780 NPs were obtained. Similarly, SP-Van NPs, SP@IR780 NPs, and CP@IR780 NPs were prepared according to the above method.

2.2.5. Van Release Kinetics. The prepared SP-Van NPs were divided into three equal parts and placed in dialysis bags. Then, the dialysis bags were placed into containers containing different buffer solutions including PBS, PBS (pH = 5.0), and GSH (10 mM + pH 5.0). The dialysis systems were placed in a shaker at 37 °C, and the dialysate was collected at specific time points. After 72 h, all samples were detected by high-performance liquid chromatography (HPLC).

2.3. In Vitro Antibacterial Activity against MRSA. **2.3.1. Minimum Inhibitory Concentration (MIC).** The minimum inhibitory concentration (MIC) values of Van and SP@IR780 NPs were tested. Briefly, TSB media (100 μL) containing drugs was dropped into a 96-well plate by 2-fold serial dilutions. MRSA (1 × 10⁶ CFU/mL, 100 μL) was added to the plate. After incubation for 24 h, the OD 600 nm of the cultures was measured with a microplate reader. Fractional inhibitory concentration index (FICI) value was calculated using the following formula:

$$FICI = \frac{MIC(AB)}{MIC(A)} + \frac{MIC(AB)}{MIC(B)}$$

MIC(AB) is the MIC of each antibacterial agent in combination (in a single well), and MIC(A) and MIC(B) are the MIC values of each antibacterial agent individually.

2.3.2. Colony Forming Units (CFU) Assay. MRSA in stationary phase was collected and diluted into 1 × 10⁶ CFU/mL in TSB. Different formulations, including PBS, Van, SP-Van NPs, CP@IR780 NPs, SP@IR780 NPs, and SP-Van@IR780 NPs, were added. The concentrations of Van and IR780 were 5 and 5 μg/mL, respectively. After incubating at 37 °C for 4 h, CP@IR780 NPs + L, SP@IR780 NPs + L, and SP-Van@IR780 NPs + L groups were irradiated under 808 nm laser at 0.5 W cm⁻² for 5 min. After being incubated at 37 °C for another 4 h, MRSA was collected and cultured on TSA.

2.3.3. CLSM of MRSA. MRSA in stationary phase was collected and diluted into 1 × 10⁹ CFU/mL in PBS. Different formulations were prepared. After incubating at 37 °C for 8 h, MRSA was collected and stained by AO/PI for 20 min. Then, the red/green fluorescence of MRSA was recorded in each group by CLSM.

2.3.4. Protein Quantitation. The protein leakage of MRSA was determined by a bicinchoninic acid (BCA) assay. MRSA in stationary phase was collected, and diluted into 1 × 10⁶ CFU/mL. Then, MRSA was treated with different formulations. After incubation at 37 °C for 8 h, 20 μL of BCA working solution was added to each well. At last, the OD540 nm of each well was recorded by a microplate reader. The amount of protein leakage from each group could be calculated from the BCA standard curve, and Ripa lysate was used as a positive control.

2.4. In Vitro Biofilm Ablation.

2.4.1. Permeability Evaluation. MRSA in the stationary phase (1 × 10⁸ CFU/mL, 1 mL) was added into a 48-well plate. After incubating at 37 °C for 24 h, the supernatant was replaced by 1 mL of fresh TSB medium. The mature biofilm was obtained after being incubated for another 24 h. The mature biofilm was treated with SP-Van@NR NPs for 0, 1, and 4 h. After cocubation, the medium was removed and the biofilm was washed with PBS three times. AO dye was added to each well to label the live bacteria. The final concentration of AO was 5 μg/mL. At last, the red/green fluorescence of the biofilm was recorded by CLSM.

2.4.2. Crystal Violet Staining. Crystal violet staining method was used to evaluate the ablation effect of SP-Van@IR780 NPs on biofilms *in vitro*. In brief, mature biofilm was treated by PBS, Van, SP-Van NPs, CP@IR780 NPs, SP@IR780 NPs, and SP-Van@IR780 NPs. After incubating at 37 °C for 4 h, CP@IR780 NPs + L, SP@IR780 NPs + L, and SP-Van@IR780 NPs + L groups were irradiated under 808 nm laser at 0.5 W cm⁻² for 5 min. After being incubated at 37 °C for another 4 h, the biofilm in each group was stained with 100 μL 1% (w/v) crystal violet for 15 min. After being washed with PBS three times, the biofilm was ablated with 100 μL 30% (v/v) acetic acid solution. At last, the OD570 nm values of the solutions in all group were measured by a microplate reader.

2.4.3. CLSM of MRSA Biofilm. Mature biofilm was incubated with different formulas. After treatment, AO and PI were added to the wells to stain the live and dead bacteria, respectively. Finally, the red/green fluorescence of the biofilm was recorded by CLSM. Software Comstat2 and ImageJ (www.comstat.dk) were used for image analysis.^{42,43}

2.5. In Vivo Antibacterial Evaluation.

2.5.1. Mice Treatment. Balb/c female mice (5–6 weeks old) were purchased from Beijing Vital River Laboratory Animal Technology Co., Ltd. All animals were treated and cared for in accordance with the National Research Council's guidelines for the care and use of laboratory animals and under the supervision and assessment by the SPF Animal Department of Clinical Institute in China–Japan Friendship Hospital (Approval No. zryhyy 12–20–08–3).

2.5.2. In Vivo Therapy. MRSA (5 × 10⁸ CUF) was injected into the subcutaneous tissue of the right leg of mice. The white abscess was observed after 1 day, and the 15 mice were equally divided into five groups with three mice in each group. Different drugs, including Van, SP-Van NPs, SP@IR780 NPs, and SP-Van@IR780 NPs, were administered to the model mice by intravenous injection, and PBS was used as a control group. The concentrations of Van and IR780 were 5 mg/kg each. At 24 and 48 h after drug injection, the wound of

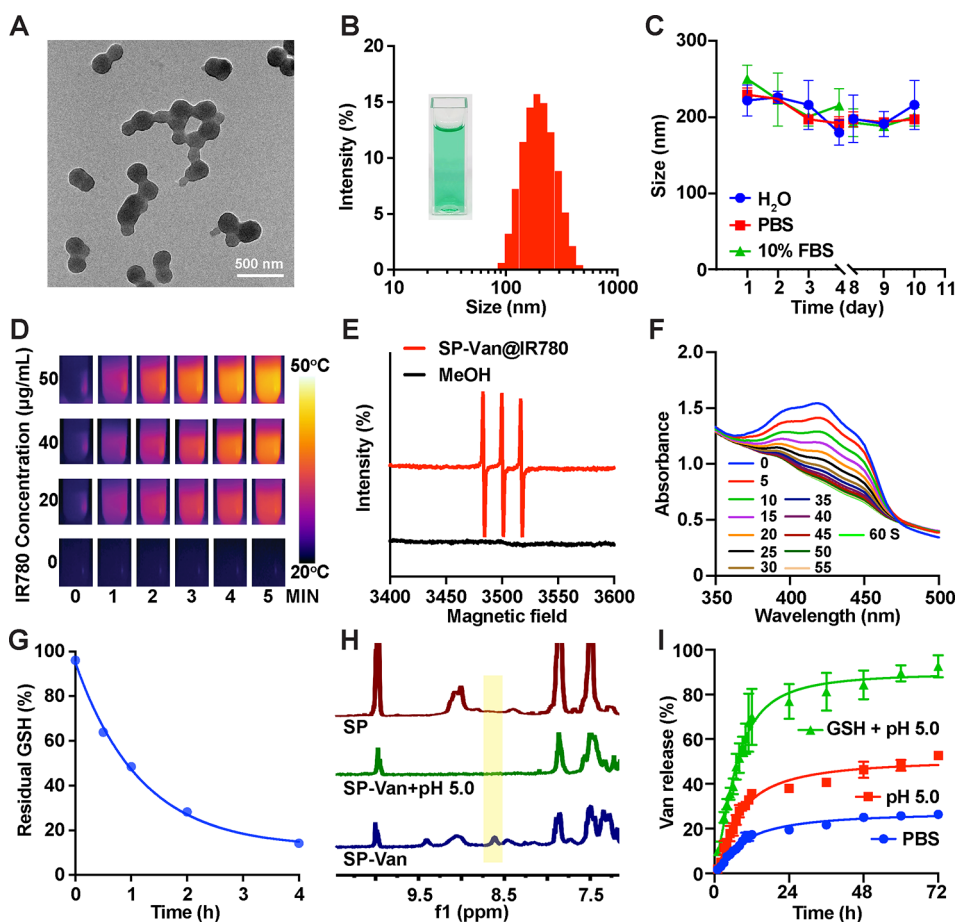


Figure 1. Characterization of SP–Van@IR780 NPs. (A) TEM image, (B) particle size distribution, and (C) particle size stability ($n = 3$) of SP–Van@IR780 NPs. (D) Thermal imaging of SP–Van@IR780 NPs irradiated by 808 nm laser at $0.5 \text{ W}\cdot\text{cm}^{-2}$ for 5 min. (E) Electron spin resonance (ESR) spectra of SP–Van@IR780 NPs irradiated by 808 nm laser at $0.5 \text{ W}\cdot\text{cm}^{-2}$ for 5 min. (F) Time-dependent absorbance spectrum of DPBF in SP–Van@IR780 NPs irradiated by 808 nm laser at $0.5 \text{ W}\cdot\text{cm}^{-2}$. (G) GSH residual rates at different times of incubation with SP@IR780 NPs by the OPA method. (H) ^1H NMR spectra of SP, SP–Van, and SP–Van in an acid environment ($\text{DMSO}-d_6$, 400 Hz). (I) Van release profiles from SP–Van NPs in different media.

mice in SP@IR780 NPs + L and SP–Van@IR780 NPs + L groups were irradiated with 808 nm laser at $0.5 \text{ W}\cdot\text{cm}^{-2}$ for 5 min. During the treatment, the wound area and body weight of the mice were recorded.

2.6. Biosafety Evaluation. **2.6.1. Hemolytic Test.** Fresh mouse eyeball blood was washed three times with PBS to obtain red blood cells, which were prepared into a 2% (v/v) suspension in PBS. SP–Van NPs were added in the concentrations of 0.125, 0.25, 0.5, 1, 2, and 4 mg/mL. The equal volumes of 10% (v/v) Triton solution and PBS were used as control groups. After incubating for 3 h at room temperature, the solutions were centrifuged at 15 000 rpm for 10 min. Finally, OD 560 nm of the supernatant was recorded by a microplate reader.

2.6.2. MTT Assay. The biocompatibility of SP–Van was evaluated using mouse fibroblast (L929 cell). L929 cell suspension was added to a 96-well plate (8000 cell/well). After incubation overnight, SP–Van NPs were added at concentrations of 7.8125, 15,625, 31.25, 62.5, 125, 250, and 500 $\mu\text{g}/\text{mL}$. After treatment for 24 h, the MTT assay was performed to examine the cell viability.

2.6.3. In Vivo Biosafety. Healthy Balb/c female mice (5–6 weeks) were divided into five groups. Different formulations, including PBS, Van, SP–Van NPs, SP@IR780 NPs, and SP–Van@IR780 NPs, were administered by intravenous injection. The concentrations of Van and IR780 were 5 mg/kg each. At day 7 of treatment, the major organs of mice were collected for hematoxylin–eosin (H&E) staining.

3. STATISTICAL ANALYSIS

The statistical method used to analyze the results was the Student's t test, and the results were expressed as mean \pm standard deviation.

4. RESULTS AND DISCUSSIONS

4.1. Characterization of Polymers and Nanoparticles.

The synthesis route of SP is shown in Scheme S1. First, a polymer, poly(CHTA-co-HD)-PEG (named as SP–COOH), which has disulfide bonds and paired carboxyl pendants, was synthesized according to our previous studies.^{44,45} According to the ^1H NMR, the molecular weight (Mw) of SP–COOH was $\sim 18\,000 \text{ g}\cdot\text{mol}^{-1}$ (Figure S1). The carboxyl groups of the SP–COOH side chain pendants were derivatized to aldehyde groups by esterification with *p*-hydroxybenzaldehyde, resulting in a polymer denoted as SP. ^1H NMR confirmed that the number of *p*-hydroxybenzaldehyde unit was ~ 15 (Figure S2). Further, Van was grafted to the SP side chain (denoted as SP–Van) by the Schiff base reaction, which was confirmed by ^1H NMR that a new peak belonging to the Schiff base bond appeared at 8.47 ppm (Figure S3).

Subsequently, SP–Van@IR780 NPs were prepared by self-assembling of SP–Van in a solvent system of DMSO/water containing IR780. Van and IR780 were detected in SP–Van@

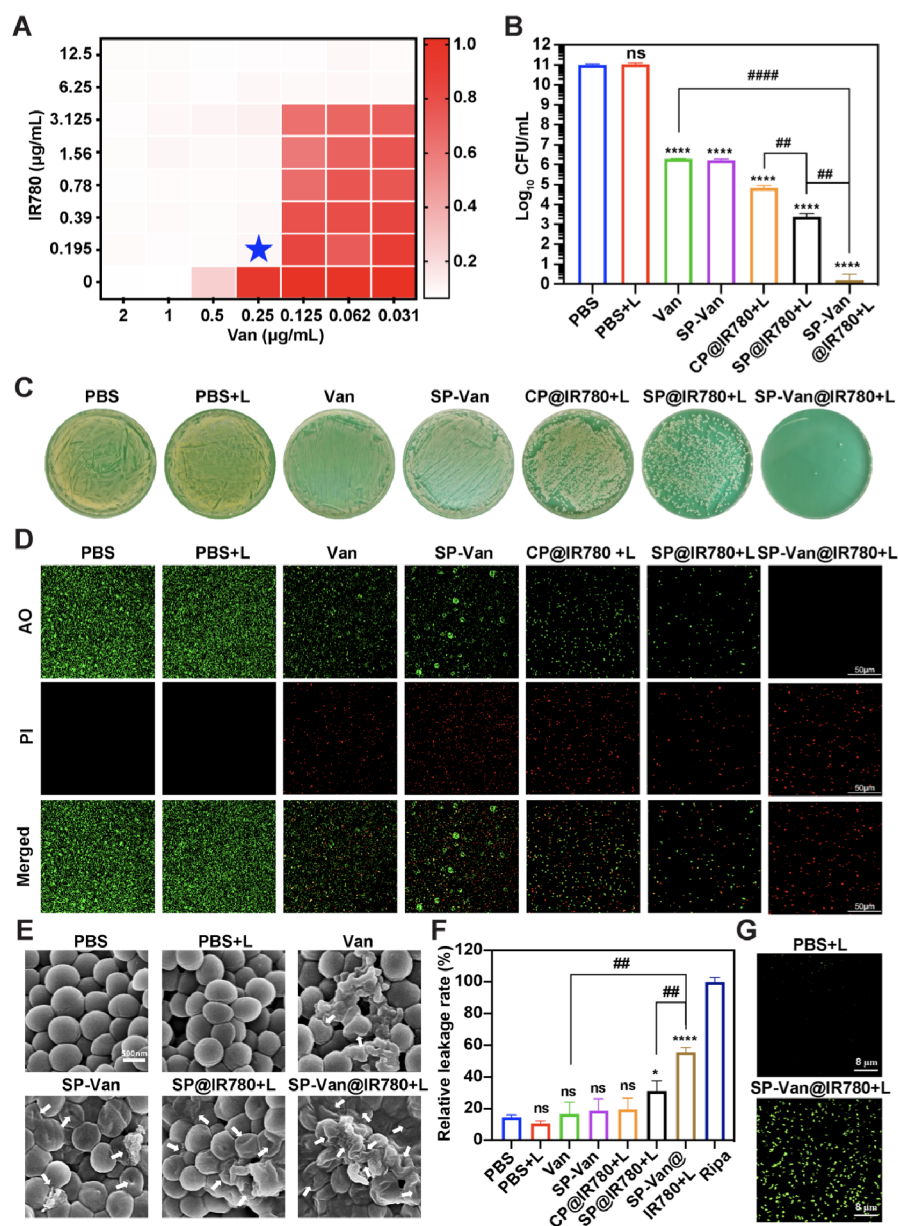


Figure 2. *In vitro* antibacterial activity of SP–Van@IR780 NPs against MRSA. (A) The synergistic antibacterial activity of Van and IR780 determining by checkerboard method, the FICI value was confirmed to be 0.28. (B) Colony-forming units (CFUs) and (C) photos of MRSA treated with various formulas for 8 h in TSB medium. (D) Confocal images of AO/PI-labeled MRSA after incubation with different drugs for 8 h. (E) SEM images of MRSA treated with various groups for 8 h, the white arrows represent sites of bacterial damage. (F) The protein leakage rate from MRSA with various treatments. (G) Confocal images of ROS in MRSA after different treatments detected by DCFH-DA probes. # means the contrasts between experimental groups and PBS. ##/**p* < 0.05, ###/***p* < 0.01, ####/*****p* < 0.001, ******p* < 0.0001, and ns *p* > 0.05, respectively.

IR780 NPs with a stable dual-drug ratio of 1:1, and the drug loading ratio was 11.1% (Figure S4). The TEM image exhibited uniform spherical SP–Van@IR780 NPs with an average size of about 199 nm (Figure 1A). The DLS test results showed that the hydrodynamic diameter and zeta potential of the SP–Van@IR780 NPs were ~230 and 15.77 mV, respectively (Figures 1B, S5). Due to the shrinkage of the nanoparticles in the dry state during TEM sample preparation, the average size from TEM image was smaller than the hydrodynamic diameters measured by DLS.^{46–48} The size stability of SP–Van@IR780 NPs in a normal physiological environment was evaluated. As shown in Figure 1C, there was no obvious change in the particle size within 10 days,

indicating that the SP–Van@IR780 NPs would have good stability in the *in vivo* circulation.

Under laser irradiation, IR780 molecules have dual functions of PTT and PDT.⁴⁹ Therefore, the temperature variation and generated ROS of SP–Van@IR780 NPs under laser irradiation were explored. After being irradiated with 808 nm laser at 0.5 W·cm⁻² for 5 min, the temperature of SP–Van@IR780 NPs (50 μg/mL) rose to 45.3 °C (Δ*t* = 12.5 °C, Figure 1D). This implied low-temperature photothermal performance of SP–Van@IR780 NPs, which could not cause damage to normal tissue.⁵⁰ Electron spin resonance (ESR) testing results confirmed that SP–Van@IR78 NPs produced a strong singlet oxygen (¹O₂) signal peak (Figure 1E). 1,3-Diphenylisobenzofuran (DPBF) was subsequently used to quantify the process

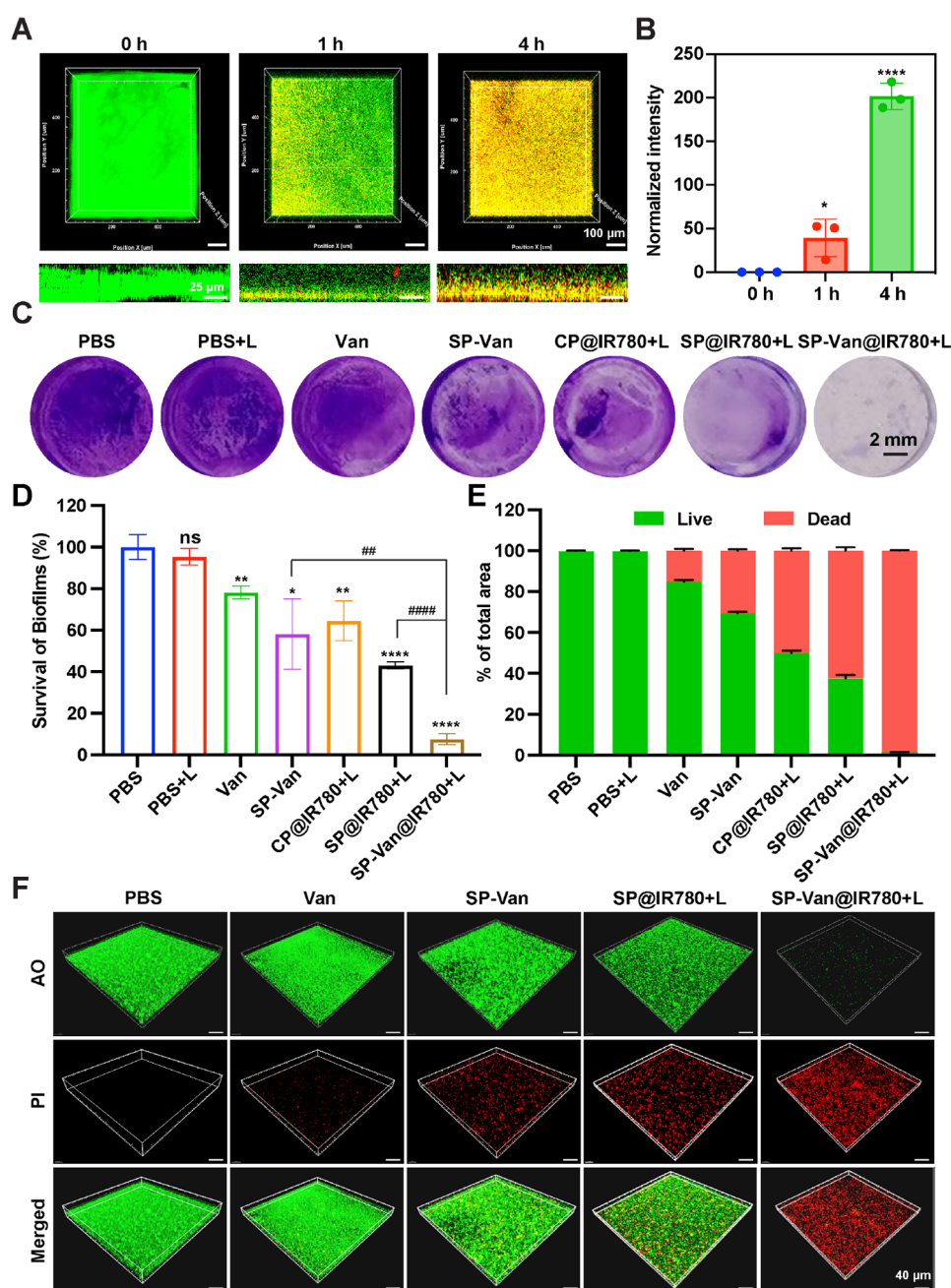


Figure 3. *In vitro* elimination activity of SP–Van@IR780 NPs on MRSA biofilms. (A) Confocal images of SP–Van@NR NPs permeation in biofilms over time. (B) Normalized intensity of red fluorescence in the cross-sectional area of the biofilm. (C) Crystal violet-stained photographs and (D) relative survival statistics of biofilms after different treatments. (E) The red/green fluorescence analysis of MRSA treated with different drugs. (F) Corresponding confocal images of MRSA with different treatments. * means the contrasts between experimental groups and PBS. #/* $p < 0.05$, ** $p < 0.01$, ### $p < 0.001$, **** $p < 0.0001$, and ns $p > 0.05$, respectively.

of $^1\text{O}_2$ generated by SP–Van@IR78 NPs. As shown in Figure 1F, with the prolongation of the laser irradiation time, the absorption peak of DPBF at 410 nm decreased rapidly within 1 min, indicating that SP–Van@IR780 NPs had excellent photodynamic performance.

SP polymer contains disulfide bonds, which can consume overexpressed GSH in the microenvironment of bacterial infection, thereby enhancing the effect of PDT.^{51,52} To confirm this hypothesis, the *o*-phthalaldehyde (OPA) derivative method was used to detect the consumption of GSH by the SP polymer. As shown in Figure 1G, the concentration of GSH rapidly decreased when GSH was coincubated with SP over

time. This implied that disulfide bonds in SP could effectively consume GSH. Conversely, as a control, CP polymer that contained “carbon–carbon” bonds instead of disulfide bonds failed to consume GSH (Scheme S2, Figures S6 and S7). The concentration of GSH did not change over time in the presence of CP polymer.⁵³ Thereby, a DPBF probe was used to test the ROS yields of SP@IR780 NPs and CP@IR780 NPs. The results showed that SP@IR780 NPs produced more ROS than CP@IR780 NPs under laser irradiation (Figure S8), further confirming that SP could consume GSH and amplify oxidative stress to sensitized PDT.

Van was coupled with the side chain of SP via Schiff base bonds to achieve responsive detachment under acidic conditions. ^1H NMR spectroscopy was used to verify the cleavage behavior of SP–Van Schiff base under acidic conditions. It showed that the characteristic peak of Schiff base around 8.4–8.5 ppm disappeared under acidic conditions (Figure 1H). The size changes of SP–Van@IR780 NPs after incubation in GSH and acidic conditions were evaluated. TEM images and DLS results showed that SP–Van@IR780 NPs could decompose into small particles of ~ 21.6 nm in size (Figure S9), which was attributed to the responsiveness of NPs to GSH and low pH. SP–Van could self-assemble into nanoparticles in the DMSO/water system. Then, the release rates of Van from SP–Van NPs in various media were then measured. As shown in Figure 1I, the cumulative release of Van was only about 20% in the pH 7.4 group at 72 h, while the release of Van in the pH 5.0 group and 10 mM GSH + pH 5.0 group exceeded 40% and 80%, respectively. Meanwhile, the release of IR780 from SP–Van@IR780 NPs was also recorded (Figure S10). IR780 showed a slow release in PBS, while it exhibited a quick release in the groups of pH 5.0 and 10 mM GSH + pH 5.0. At 72 h, the cumulative release rates of IR780 in the PBS, pH 5.0, and GSH + pH 5.0 groups were 21%, 49%, and 89%, respectively. These results suggested that SP–Van NPs could avoid the leakage of Van when it is in a normal biological environment, while the Van would realize responsive release once SP–Van NPs reached the acidic and high GSH environment of the bacterial infection site.

4.2. In Vitro Antibacterial Activity of SP–Van@IR780 NPs against MRSA. *In vitro* antibacterial activity of SP–Van@IR780 NPs against MRSA was then investigated. First, the dosage ratio between Van and IR780 in SP@IR780 NPs was confirmed by check-box experiments (Figure 2A). Under mild irradiation ($0.5\text{ W}\cdot\text{cm}^{-2}$, 808 nm laser irradiation for 5 min), IR780 showed a minimal inhibitory concentration (MIC) at $6.25\ \mu\text{g}/\text{mL}$. When IR780 ($0.195\text{--}3.125\ \mu\text{g}/\text{mL}$) was used together with Van, even though the concentration of IR780 was below the MIC, its phototherapy effects could significantly reinforce the antibacterial performance of Van. The FICI value between Van and IR780 was $0.28\text{--}0.5$ ($\text{FICI} \leq 0.5$ indicates synergy, $0.5 < \text{FICI} \leq 4.0$ indicates indifference and $\text{FICI} > 4.0$ indicates antagonism).⁵⁴ Specially, when IR780 was set as $0.195\ \mu\text{g}/\text{mL}$ and Van was $0.25\ \mu\text{g}/\text{mL}$, the FICI was 0.28 (Figures 2A, S11), fully indicating the strong synergistic antibacterial effect of low-dose phototherapy and Van.

Accordingly, SP–Van@IR780 NPs were fabricated with Van and IR780 in a synergistic dose ratio ($C_{(\text{Van})} = 5\ \mu\text{g}/\text{mL}$, $C_{(\text{IR780})} = 5\ \mu\text{g}/\text{mL}$). Bactericidal assay revealed that the obtained SP–Van@IR780 NPs under laser irradiation (808 nm, $0.5\text{ W}\cdot\text{cm}^{-2}$, 5 min; denoted as SP–Van@IR780 NPs + L) could exceedingly killed 99.99999% (****, $p = 0.000001$) planktonic MRSA (Figure 2B–D), which was in agreement with the checkboard experiments. Conversely, antibiotic therapy (Van and SP–Van NPs) and phototherapy (CP@IR780 NPs + L and SP@IR780 NPs + L) failed to eliminate MRSA at the same dose. Only when the concentrations of Van and SP@IR780 NPs were up to 60 and 20 $\mu\text{g}/\text{mL}$, respectively, could they achieve a comparable bactericidal effect as SP–Van@IR780 NPs (Figure S12). That is, SP–Van@IR780 NPs significantly reduced the required dosage of Van and SP@IR780 NPs by 83.33% and 50.00%, respectively. Interestingly, SP@IR780 NPs + L exhibited better bactericidal

efficacy than CP@IR780 NPs + L (##, $p < 0.01$). This was mainly due to disulfide bonds in SP@IR780 NPs depleting GSH and increased accumulation of ROS (Figure S8). This accumulated ROS could alter bacterial electronic respiration, amplify the oxidative stress, and, consequently, sensitize the bactericidal effect.⁵⁵

SEM observation of bacterial morphology exhibited varying degrees of visible damage (white arrows in Figure 2E) of the bacteria in the groups of antibiotic therapy (Van and SP–Van NPs) and phototherapy (CP@IR780 NPs + L and SP@IR780 NPs + L). Comparatively, almost all bacteria within the field of view showed extreme deformation in the SP–Van@IR780 NPs + L group. Further, the BCA assay confirmed that the relative protein leakage rate of the bacteria in SP–Van@IR780 NPs + L group was nearly four times higher than that of the PBS group (****, $p < 0.0001$, Figure 2F) and showed significant differences compared to the groups of SP@IR780 NPs + L (##, $p = 0.0037$) and Van (##, $p = 0.0011$). This stark damaging effect on MRSA would be caused by the synergistic effects of antibiotic therapy and phototherapy. Thereafter, a specific fluorescent probe (2',7'-dichlorofluorescein diacetate, DCFH-DA) was used for detecting bacterial ROS. Compared with untreated MRSA, the MRSA treated by SP–Van@IR780 NPs + L produced high doses of fatal ROS (Figure 2G). Taken together, these experimental results supported striking antibacterial performance of SP–Van@IR780 NPs, which involves synergistic enhancements of PDT/PTT and antibiotic therapy.

4.3. In Vitro Antibiofilm Activity of SP–Van@IR780 NPs. Penetration restriction is the primary challenge for the antibiotic treatment of biofilms. To explore the permeability of NPs in biofilms, we recorded the penetration of SP–Van@NR NPs (red fluorescence) into AO-labeled biofilms (green fluorescence) using CLSM without adjunct phototherapy. After coincubating SP–Van@NR NPs separately with biofilms for 0, 1, and 4 h, a gradual penetration of the NPs into the interior of the biofilms was observed (Figure 3A). Quantitative analysis using software *ImageJ* further demonstrated that the red fluorescence (the NPs) in the cross-sections of biofilms sharply increased over time, suggesting that the NPs could successfully penetrate into biofilms (Figure 3B).

Subsequently, their ability to eliminate MRSA biofilms was characterized through a crystal violet staining assay (Figure 3C,D). Compared with the naked Van, SP–Van did show reinforced elimination capacity because of its incremental penetration of biofilm; however the capacity of SP–Van was limited. This could be attributed to the fact that dormant or semidormant bacteria in biofilms can withstand high-dose antibiotics. In this regard, PDT/PTT could be a potential mean to exert redox activity to fight against these opportunistic bacteria. As shown in Figure 3D, SP@IR780 NPs + L had a higher biofilm elimination rate than Van and SP–Van. Consistent with the trend of *in vitro* anti-MRSA experiment results, the SP@IR780 NPs + L group had a higher biofilm elimination rate (56.90%) than the CP@IR780 NPs + L group (35.59%) because of the increased consumption of GSH by disulfide bonds and increased accumulation of ROS. Importantly, the SP–Van@IR780 NPs + L group, which combined phototherapy and antibiotic therapy, could achieve the highest biofilm elimination rate, which was up to 92.43% (****, $p = 0.000017$). To visualize the ability of NPs to eliminate biofilms, the live/dead (AO/PI) staining assay of bacterial biofilms treated with different drugs was carried out

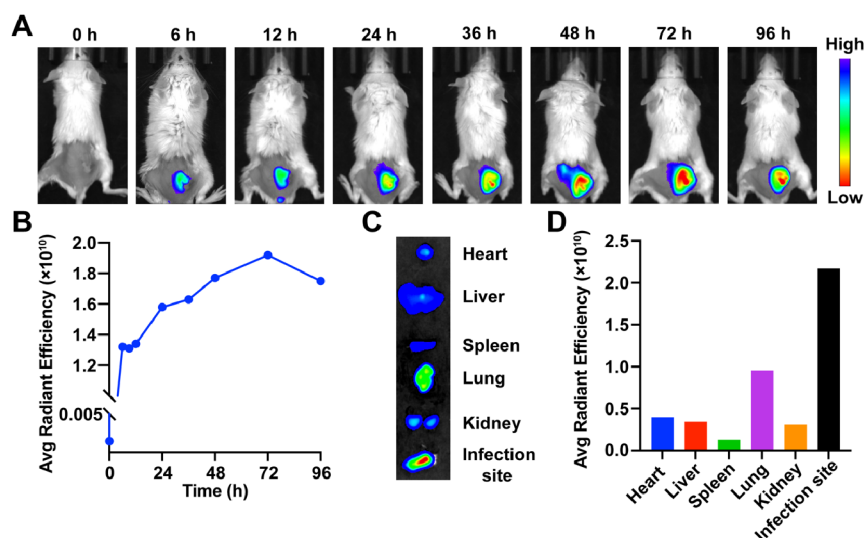


Figure 4. (A) Images of fluorescence distribution in mice after intravenous injection of SP–Van@IR780 NPs. (B) Variation of fluorescence intensity at the site of subcutaneous abscesses in mice over time. (C) Fluorescence images of isolated organs and wound tissue from mice at 72 h after SP–Van@IR780 NPs injection (*i. v.*) and (D) the corresponding analysis of fluorescence intensity of the tissues.

(Figure 3E,F). Quantitative analysis showed that the red fluorescence of SP–Van@IR780 NPs + L group was 98.8% of the total area, which was better than those of SP@IR780 (62.5%), CP@IR780 (50.0%), SP–Van (30.6%), and Van (15.0%) groups. Meanwhile, the thickness of the biofilm in PBS group was calculated to be 24 μm . When the biofilm was treated with Van and SP–Van NPs, the thickness of the biofilm slightly decreased to 18 and 15 μm , respectively. Phototherapy showed better biofilm-elimination efficacy than antibiotics, in which CP@IR780 NPs + L and SP@IR780 NPs + L treatments decreased the thickness of the biofilm to be 10 and 9 μm , respectively. In contrast, SP–Van@IR780 NPs + L exhibited the best performance, and only 0.3 μm -thick biofilm remained. These results fully indicated that mild phototherapy effectively sensitized antibiotics to improve their ability to eliminate biofilms. In this case, the structure of SP–Van@IR780 NPs is critical for exerting its synergistic effect. There was high GSH in biofilm infection environment, and pH values gradually decreased from the exterior to the interior of biofilm. Under these conditions, the disulfide bonds in SP–Van@IR780 NPs could first break because of the high concentration of GSH. The NPs were then reduced in size and disintegrated to achieve deep biofilm penetration. Meanwhile, IR780 released from NPs upon disintegration produced heat and ROS under NIR irradiation to destroy EPS and resuscitated the bacteria that reside inside the biofilm and possess low metabolic activity. After penetrating into the interior of biofilm, the Schiff bases bonds in SP–Van@IR780 NPs broke at low pH. Van was then detached from the NPs to kill the inner bacteria and eliminate the biofilm. Therefore, SP–Van@IR780 NPs could effectively exert the synergistic effect of low-dose phototherapy and Van via the introduction of disulfide bonds and Schiff bases bonds.

4.4. In Vivo Distribution of SP–Van@IR780 NPs. After confirming the ability of SP–Van@IR780 NPs to eradicate MRSA and biofilms *in vitro*, the *in vivo* antimicrobial efficacy of SP–Van@IR780 NPs was aimed to evaluate utilizing a mouse subcutaneous abscess model.⁵⁶ Following intravenous injection of SP–Van@IR780 NPs into the tail vein, an IVIS spectral *in vivo* imaging system was performed to track the distribution of

SP–Van@IR780 NPs in the mice. As shown in Figure 4A, SP–Van@IR780 NPs could be clearly detected at the infection site 6 h after drug administration. It was gradually accumulated as observation time was extended and finally reached maximum accumulation at 72 h; the accumulation of SP–Van@IR780 NPs at the infection site was still at a high level at 96 h post *i.v.* injection; only 9% fluorescence attenuation compared with that at post-72 h (Figure 4B). Further, the major organs and wound tissue of mice were isolated and observed by IVIS at 72 h after SP–Van@IR780 NPs injection. The *ex vivo* biodistribution data indicated that SP–Van@IR780 NPs were mainly distributed in the infection site, and followed by the lungs, which was likely due to a mild lung infection caused by the subcutaneous abscess model (Figure 4C,D). These results indicated that SP–Van@IR780 NPs possessed excellent targeting ability of bacterial infection because of the introduction of Van; SP–Van@IR780 NPs could significantly reduce the number of administrations, and thus, reduce the dose of antibiotics, which is critical for long-term bactericidal performance.

4.5. In Vivo Treatment of Subcutaneous Abscesses. *In vivo* antibacterial performance of SP–Van@IR780 NPs was assessed using a subcutaneous abscess model. As illustrated in Figure 5A, 5×10^8 CFU of the MRSA suspension was injected into the skin tissue of the right hind leg of mice. On the second day, the mice were randomly divided into five groups (PBS, Van, SP–Van NPs, SP@IR780 NPs + L, SP–Van@IR780 NPs + L ($n = 3$)). The corresponding drugs were intravenously injected via the vein tail and only administered once throughout the treatment. The infective sites of mice in SP@IR780 NPs + L group and SP–Van@IR780 NPs + L group were irradiated with 808 nm laser at $0.5 \text{ W}\cdot\text{cm}^{-2}$ for 5 min on the second and fourth day, respectively. Photographs of the infective sites in different treatment groups were taken on days 1, 2, 3, 5, 7, and 10 (Figure 5B). It could be clearly seen that the wounds of the mice in each group were gradually healed with the prolongation of the treatment time. Apparently, wounds in the SP–Van@IR780 NPs + L group healed first on day 10 compared to those in the remaining groups. Simulation analysis of wound healing processes in mice also visually

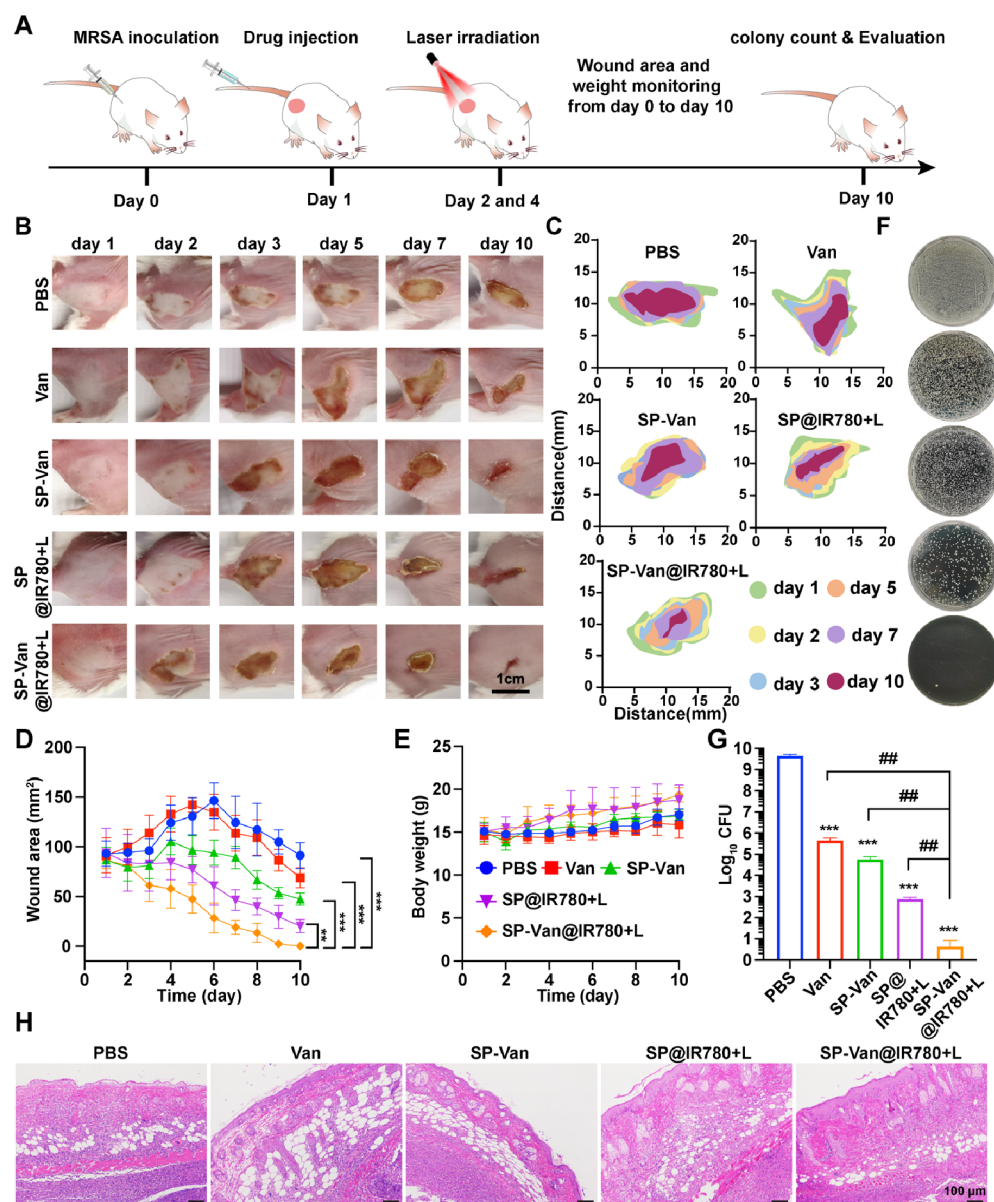


Figure 5. (A) Schematic diagram of subcutaneous abscess model construction and *in vivo* treatment studies. (B) Photographs of MRSA-infected skin of mice in each treatment group. (C) Schematic diagram that simulated the infected skin wound of mice in all groups. (D) The curves of (E) wound area and body weight of mice in each treatment group, $n = 3$. (F) Photographs of bacterial colony plates and (G) CFUs of infected skin at day 10 of treatment. (H) H&E-stained images of skin tissue from all groups at day 10 of treatment. * means the contrasts between experimental groups and PBS. **/### $p < 0.01$, *** $p < 0.001$, respectively.

illustrated the above results (Figure 5C). The curves of wound area over time for each group of mice were plotted, as shown in Figure 5D. At day 10, the wound area of SP-Van@IR780 NPs was only 0.3 mm^3 , which was significantly reduced compared with the control groups (**, $p = 0.006$ for SP@IR780 NPs + L group; 20.3 mm^3 ; ***, $p = 0.0002$ for SP-Van NPs group; 47.4 mm^3 ; ***, $p = 0.0003$ for Van group; 69.0 mm^3 ; and ***, $p = 0.003$ for PBS group; 91.3 mm^3). At the same time, the body weight of all groups during the treatment period was continuously monitored (Figure 5E). It was worth noting that the weight gain rate of the mice in the PBS, Van, and SP-Van groups was smaller than those in the SP@IR780 NPs + L and SP-Van@IR780 NPs + L groups, indicating that the faster the wound recovery, the more beneficial it is for the normal growth of mice. Bacterial colony of the infection sites showed that there were almost no residual bacteria in the SP-

Van@IR780 NPs + L group (Figure 5F). As shown in Figure 5G, the CFUs in SP-Van@IR780 NPs + L group were significantly lower than those in PBS, Van, SP-Van NPs, and SP@IR780 NPs + L groups (##, $p = 0.001$ for SP-Van@IR780 NPs + L group; ###, $p = 0.006$ for SP-Van NPs group; ##, $p = 0.003$ for Van group; and ***, $p = 0.0002$ for PBS group). The recovery of infected skin tissue was further assessed by hematoxylin and eosin (H&E) staining experiments (Figure 5H). The inflammatory cell infiltration was reduced in the drug-treated groups compared to the PBS group. The images of the SP-Van@IR780 NPs + L group showed the least infiltration of inflammatory cells, indicating the best tissue healing.^{57,58} These results indicated that the cascade-responsive SP-Van@IR780 NPs efficiently eliminated MRSA infection *in vivo* by amplified phototherapy and Van synergistic treatment.

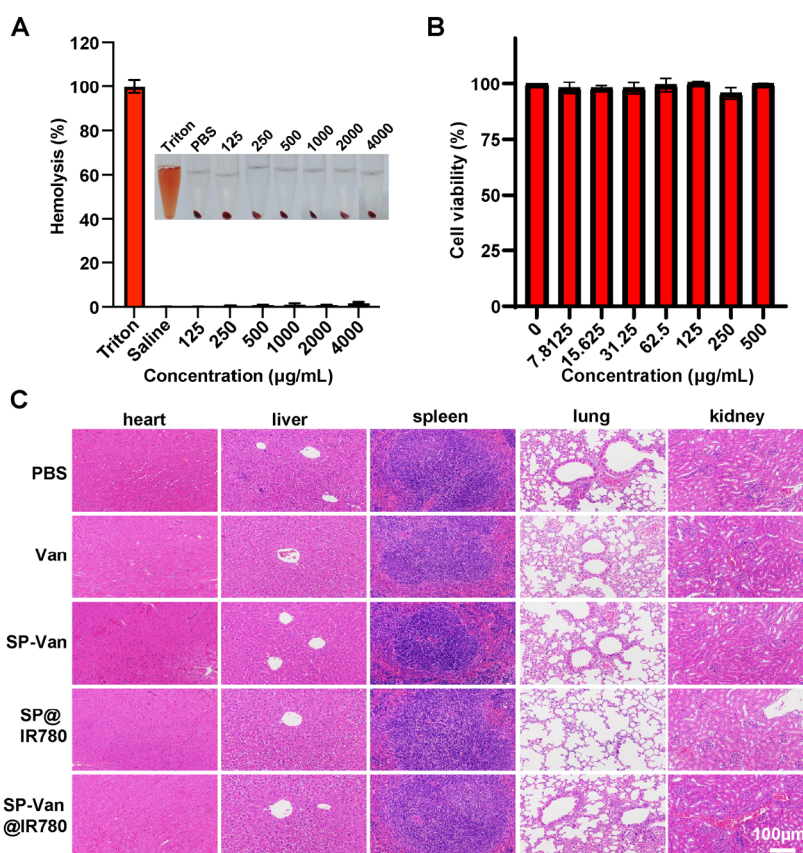


Figure 6. (A) Hemolysis of red blood cells (RBCs) by different concentrations of SP-Van. (B) The relative cell viability of L929 cells after treated with different concentrations of SP-Van for 24 h. (C) H&E staining images of major organs from healthy mice after different treatments including heart, liver, spleen, lung and kidney.

4.6. Biosafety Evaluation. The biosafety of SP-Van@IR780 NPs was eventually evaluated. Hemolysis test and MTT assay were used to examine the toxicity of SP-Van against mammalian cells. As shown in Figure 6A, the hemolysis rate of SP-Van was lower than 5% even at the concentration of 4000 $\mu\text{g/mL}$; the cell viability of L929 cells was still over 90% when the concentration of SP-Van was up to 500 $\mu\text{g/mL}$ (Figure 6B), indicating the good biocompatibility of SP-Van *in vitro*. Subsequently, healthy BALB/C mice were administered with PBS, Van, SP-Van, SP@IR780 NPs, and SP-Van@IR780 NPs by intravenous injection (*i.v.*). The hematoxylin and eosin (H&E) stainings of the major organs (including heart, liver, spleen, lung, kidney) from mice were performed and no obvious histological, morphological, or pathological abnormalities were observed in all treatment groups (Figure 6C). Therefore, SP-Van@IR780 NPs had excellent biosafety *in vitro* and *in vivo*.

5. CONCLUSION

In summary, robust SP-Van@IR780 NPs were proposed to achieve effective eradication of planktonic MRSA and biofilms. The introduction of disulfide bonds and Schiff base bonds endowed SP-Van@IR780 NPs with astonishing ability of biofilm penetration, ROS accumulation, and targeted Van delivery, which fully exerted the multifunctional advantages of SP-Van@IR780 NPs. The NPs exhibited distinctive synergistic effects of mild phototherapy and antibacterial therapy (FICI = 0.28). Under NIR irradiation, the phototherapy produced extra ROS to destroy EPS and rouse bacteria, while

the antibiotic Van was delivered to target the infection and kill the resuscitated bacteria. Both *in vitro* and *in vivo* results demonstrated that SP-Van@IR780 NPs possessed appealing antibacterial performances for biofilm infection elimination. Considering the excellent biocompatibility, this study provides a reliable and effective nanoplatform for the clinical elimination of biofilm-associated infectious diseases.

ASSOCIATED CONTENT

Supporting Information

The Supporting Information is available free of charge at <https://pubs.acs.org/doi/10.1021/acsami.3c17198>.

Additional synthetic procedures and experimental data, including the data of ^1H NMR, TEM and DLS results, UV spectra, FICI value, and CFU statistics (PDF)

AUTHOR INFORMATION

Corresponding Authors

Guofeng Li – State Key Laboratory of Organic-Inorganic Composites, Beijing Laboratory of Biomedical Materials, Beijing University of Chemical Technology, Beijing 100029, PR China; orcid.org/0000-0002-4101-0059; Email: ligf@mail.buct.edu.cn

Xing Wang – State Key Laboratory of Organic-Inorganic Composites, Beijing Laboratory of Biomedical Materials, Beijing University of Chemical Technology, Beijing 100029, PR China; orcid.org/0000-0002-9990-1479; Email: wangxing@mail.buct.edu.cn

Authors

Xiaoxu Kang – State Key Laboratory of Organic–Inorganic Composites, Beijing Laboratory of Biomedical Materials, Beijing University of Chemical Technology, Beijing 100029, PR China; China-Japan Friendship Hospital, Beijing 100029, PR China

Xuankun Yang – State Key Laboratory of Organic–Inorganic Composites, Beijing Laboratory of Biomedical Materials, Beijing University of Chemical Technology, Beijing 100029, PR China

Fanqiang Bu – State Key Laboratory of Organic–Inorganic Composites, Beijing Laboratory of Biomedical Materials, Beijing University of Chemical Technology, Beijing 100029, PR China

Wenli Feng – State Key Laboratory of Organic–Inorganic Composites, Beijing Laboratory of Biomedical Materials, Beijing University of Chemical Technology, Beijing 100029, PR China

Fang Liu – China-Japan Friendship Hospital, Beijing 100029, PR China

Wensheng Xie – State Key Laboratory of Organic–Inorganic Composites, Beijing Laboratory of Biomedical Materials, Beijing University of Chemical Technology, Beijing 100029, PR China

Complete contact information is available at:
<https://pubs.acs.org/10.1021/acsami.3c17198>

Author Contributions

[§]The authors contributed equally. All authors have given approval to the final version of the manuscript.

Notes

The authors declare no competing financial interest.

ACKNOWLEDGMENTS

X.W. and G.L. thank the National Natural Science Foundation of China (nos. 22275013, 52273118, and 22005020) and Joint Project of BRC-BC (Biomedical Translational Engineering Research Center of BUCT-CJFH) (no. XK2023-16).

REFERENCES

- (1) GBD 2019 Antimicrobial Resistance Collaborators. Global Mortality Associated with 33 Bacterial Pathogens in 2019: A Systematic Analysis for the Global Burden of Disease Study 2019. *Lancet* **2022**, *400* (10369), 2221–2248.
- (2) Stracy, M.; Snitser, O.; Yelin, I.; Amer, Y.; Parizade, M.; Katz, R.; Rimler, G.; Wolf, T.; Herzel, E.; Koren, G.; Kuint, J.; Foxman, B.; Chodick, G.; Shalev, V.; Kishony, R. Minimizing Treatment-Induced Emergence of Antibiotic Resistance in Bacterial Infections. *Science* **2022**, *375* (6583), 889–894.
- (3) Mitcheltree, M. J.; Pisipati, A.; Syroegin, E. A.; Silvestre, K. J.; Klepacki, D.; Mason, J. D.; Terwilliger, D. W.; Testolin, G.; Pote, A. R.; Wu, K. J.; Ladley, R. P.; Chatman, K.; Mankin, A. S.; Polikanov, Y. S.; Myers, A. G. A Synthetic Antibiotic Class Overcoming Bacterial Multidrug Resistance. *Nature* **2021**, *599* (7885), 507–512.
- (4) Zhang, W.; Zhou, Y.; Fan, Y.; Cao, R.; Xu, Y.; Weng, Z.; Ye, J.; He, C.; Zhu, Y.; Wang, X. Metal–Organic–Framework–Based Hydrogen–Release Platform for Multieffective *Helicobacter Pylori* Targeting Therapy and Intestinal Flora Protective Capabilities. *Adv. Mater.* **2022**, *34* (2), No. e2105738.
- (5) Feng, W.; Li, G.; Kang, X.; Wang, R.; Liu, F.; Zhao, D.; Li, H.; Bu, F.; Yu, Y.; Moriarty, T. F.; Ren, Q.; Wang, X. Cascade-Targeting Poly(amino acid) Nanoparticles Eliminate Intracellular Bacteria via On-Site Antibiotic Delivery. *Adv. Mater.* **2022**, *34* (12), No. e2109789.
- (6) Darby, E. M.; Trampari, E.; Siasat, P.; Gaya, M. S.; Alav, I.; Webber, M. A.; Blair, J. M. Molecular Mechanisms of Antibiotic Resistance Revisited. *Nat. Rev. Microbiol.* **2023**, *21* (5), 280–295.
- (7) Ding, X.; Yang, C.; Moreira, W.; Yuan, P.; Periaswamy, B.; de Sessions, P. F.; Zhao, H.; Tan, J.; Lee, A.; Ong, K. X.; Park, N.; Liang, Z. C.; Hedrick, J. L.; Yang, Y. Y. A Macromolecule Reversing Antibiotic Resistance Phenotype and Repurposing Drugs as Potent Antibiotics. *Adv. Sci.* **2020**, *7* (17), 2001374.
- (8) Wei, T.; Yu, Q.; Chen, H. Responsive and Synergistic Antibacterial Coatings: Fighting against Bacteria in a Smart and Effective Way. *Adv. Healthcare Mater.* **2019**, *8* (3), 1801381.
- (9) Vestby, L. K.; Grønseth, T.; Simm, R.; Nesse, L. L. Bacterial Biofilm and Its Role in the Pathogenesis of Disease. *Antibiotics* **2020**, *9* (2), 59.
- (10) Ran, M.; Gounani, Z.; Yan, J.; Rosenholm, J. M.; Zhang, H. Ca²⁺ Enhanced Photosensitizer/Dnase I Nanocomposite Mediated Bacterial Eradication Through Biofilm Disruption and Photothermal Therapy. *Nano Select* **2022**, *3* (7), 1201–1211.
- (11) Vitale, S.; Rampazzo, E.; Hiebner, D.; Devlin, H.; Quinn, L.; Prodi, L.; Casey, E. Interaction Between Engineered Pluronic Silica Nanoparticles and Bacterial Biofilms: Elucidating the Role of Nanoparticle Surface Chemistry and EPS Matrix. *ACS Appl. Mater. Interfaces* **2022**, *14* (30), 34502–34512.
- (12) Davies, D. Understanding Biofilm Resistance to Antibacterial Agents. *Nat. Rev. Drug Discovery* **2003**, *2* (2), 114–122.
- (13) Hu, D.; Zou, L.; Gao, Y.; Jin, Q.; Ji, J. Emerging Nanobiomaterials Against Bacterial Infections in Postantibiotic Era. *View* **2020**, *1* (3), 20200014.
- (14) Jo, J.; Price-Whelan, A.; Dietrich, L. E. P. Gradients and Consequences of Heterogeneity in Biofilms. *Nat. Rev. Microbiol.* **2022**, *20* (10), 593–607.
- (15) Stewart, P. S.; Franklin, M. J. Physiological Heterogeneity in Biofilms. *Nat. Rev. Microbiol.* **2008**, *6* (3), 199–210.
- (16) Xiu, W.; Wan, L.; Yang, K.; Li, X.; Yuwen, L.; Dong, H.; Mou, Y.; Yang, D.; Wang, L. Potentiating Hypoxic Microenvironment for Antibiotic Activation by Photodynamic Therapy to Combat Bacterial Biofilm Infections. *Nat. Commun.* **2022**, *13* (1), 3875.
- (17) Fisher, R. A.; Gollan, B.; Helaine, S. Persistent Bacterial Infections and Persister Cells. *Nat. Rev. Microbiol.* **2017**, *15* (8), 453–464.
- (18) Wei, G.; Yang, G.; Wang, Y.; Jiang, H.; Fu, Y.; Yue, G.; Ju, R. Phototherapy-Based Combination Strategies for Bacterial Infection Treatment. *Theranostics* **2020**, *10* (26), 12241.
- (19) Zhou, S.; Wang, Z.; Wang, Y.; Feng, L. Near-Infrared Light-Triggered Synergistic Phototherapy for Antimicrobial Therapy. *ACS Appl. Bio Mater.* **2020**, *3* (3), 1730–1737.
- (20) Wang, Y.; Jin, Y.; Chen, W.; Wang, J.; Chen, H.; Sun, L.; Li, X.; Ji, J.; Yu, Q.; Shen, L.; Wang, B. Construction of Nanomaterials with Targeting Phototherapy Properties to Inhibit Resistant Bacteria and Biofilm Infections. *Chem. Eng. J.* **2019**, *358*, 74–90.
- (21) Zhang, J.; Jia, Q.; Yue, Z.; Huo, J.; Chai, J.; Yu, L.; Nie, R.; Shao, H.; Zhao, Y.; Li, P.; Huang, W. An Electroluminescence Flexible Device for Highly Efficient Eradication of Drug-Resistant Bacteria. *Adv. Mater.* **2022**, *34* (17), No. e2200334.
- (22) Ran, M.; Sun, R.; Yan, J.; Pulliainen, A. T.; Zhang, Y.; Zhang, H. DNA Nanoflower Eye Drops with Antibiotic-Resistant Gene Regulation Ability for MRSA Keratitis Target Treatment. *Small* **2023**, *19* (47), No. e2304194.
- (23) Xie, Z.; Fan, T.; An, J.; Choi, W.; Duo, Y.; Ge, Y.; Zhang, B.; Nie, G.; Xie, N.; Zheng, T.; Chen, Y.; Zhang, H.; Kim, J. S. Emerging Combination Strategies with Phototherapy in Cancer Nanomedicine. *Chem. Soc. Rev.* **2020**, *49* (22), 8065–8087.
- (24) Qiao, Y.; Ma, Y.; Tong, Y.; Liu, W.; Wang, S.; Zheng, Y.; Men, C.; Yu, J.; Pan, J.; Wan, D.; Yin, Y.; Zhao, X.; Xi, R.; Meng, M. Phototherapy and Mechanism Exploration of Biofilm and Multidrug-Resistant *Helicobacter pylori* by Bacteria-Targeted NIR Photosensitizer. *Small* **2023**, *19* (4), No. e2205248.

- (25) Deng, X.; Shao, Z.; Zhao, Y. Solutions to the Drawbacks of Photothermal and Photodynamic Cancer Therapy. *Adv. Sci.* **2021**, *8* (3), 2002504.
- (26) Hu, Y.; Ruan, X.; Lv, X.; Xu, Y.; Wang, W.; Cai, Y.; Ding, M.; Dong, H.; Shao, J.; Yang, D.; Dong, X. Biofilm Microenvironment-Responsive Nanoparticles for the Treatment of Bacterial Infection. *Nano Today* **2022**, *46*, 101602.
- (27) Xu, M.; Hu, Y.; Xiao, Y.; Zhang, Y.; Sun, K.; Wu, T.; Lv, N.; Wang, W.; Ding, W.; Li, F.; Qiu, B.; Li, J. Near-Infrared-Controlled Nanoplatfrom Exploiting Photothermal Promotion of Peroxidase-Like and Oxd-Like Activities for Potent Antibacterial and Anti-Biofilm Therapies. *ACS Appl. Mater. Interfaces* **2020**, *12* (45), 50260–50274.
- (28) Yang, L.; Zhang, D.; Li, W.; Lin, H.; Ding, C.; Liu, Q.; Wang, L.; Li, Z.; Mei, L.; Chen, H.; Zhao, Y.; Zeng, X. Biofilm Microenvironment Triggered Self-Enhancing Photodynamic Immunomodulatory Microneedle for Diabetic Wound Therapy. *Nat. Commun.* **2023**, *14* (1), 7658.
- (29) Wang, J.; Zhao, S.; Chen, J.; Liu, X.; Chen, H.; Lu, T.; Xu, M.; Guo, X.; Shen, X.; Liu, C.; Li, C. Phage-Ce6-Manganese Dioxide Nanocomposite-Mediated Photodynamic, Photothermal, and Chemodynamic Therapies to Eliminate Biofilms and Improve Wound Healing. *ACS Appl. Mater. Interfaces* **2023**, *15* (18), 21904–21916.
- (30) Yang, K.; Zhao, S.; Li, B.; Wang, B.; Lan, M.; Song, X. Low Temperature Photothermal Therapy: Advances and Perspectives. *Coord. Chem. Rev.* **2022**, *454*, 214330.
- (31) Feng, Y.; Tonon, C. C.; Ashraf, S.; Hasan, T. Photodynamic and Antibiotic Therapy in Combination Against Bacterial Infections: Efficacy, Determinants, Mechanisms, and Future Perspectives. *Adv. Drug Delivery Rev.* **2021**, *177*, 113941.
- (32) Makabenta, J. M. V.; Nabawy, A.; Li, C.-H.; Schmidt-Malan, S.; Patel, R.; Rotello, V. M.; Schmidt-Malan, S.; Patel, R.; Rotello, V. M. Nanomaterial-Based Therapeutics for Antibiotic-Resistant Bacterial Infections. *Nat. Rev. Microbiol.* **2021**, *19* (1), 23–36.
- (33) Kalelkar, P. P.; Riddick, M.; García, A. J. Biomaterial-Based Antimicrobial Therapies for The Treatment of Bacterial Infections. *Nat. Rev. Mater.* **2022**, *7* (1), 39–54.
- (34) Li, Z.; Pan, W.; Shi, E.; Bai, L.; Liu, H.; Li, C.; Wang, Y.; Deng, J.; Wang, Y. A Multifunctional Nanosystem Based on Bacterial Cell-Penetrating Photosensitizer for Fighting Periodontitis via Combining Photodynamic and Antibiotic Therapies. *ACS Biomater. Sci. Eng.* **2021**, *7* (2), 772–786.
- (35) Hu, X.; Zhang, H.; Wang, Y.; Shiu, B.-C.; Lin, J.-H.; Zhang, S.; Lou, C.-W.; Li, T.-T. Synergistic Antibacterial Strategy Based on Photodynamic Therapy: Progress and Perspectives. *Chem. Eng. J.* **2022**, *450*, 138129.
- (36) Lv, B.; Huang, X.; Lijia, C.; Ma, Y.; Bian, M.; Li, Z.; Duan, J.; Zhou, F.; Yang, B.; Qie, X.; Song, Y.; Wood, T. K.; Fu, X. Heat Shock Potentiates Aminoglycosides Against Gram-Negative Bacteria by Enhancing Antibiotic Uptake, Protein Aggregation, and ROS. *Proc. Natl. Acad. Sci. U. S. A.* **2023**, *120* (12), No. e2217254120.
- (37) Lázár, V.; Snitser, O.; Barkan, D.; Kishony, R. Antibiotic Combinations Reduce *Staphylococcus aureus* Clearance. *Nature* **2022**, *610* (7932), 540–546.
- (38) Brochado, A. R.; Telzerow, A.; Bobonis, J.; Banzhaf, M.; Mateus, A.; Selkrig, J.; Huth, E.; Bassler, S.; Zamarreno Beas, J.; Zietek, M.; Ng, N.; Foerster, S.; Ezratty, B.; Py, B.; Barras, F.; Savitski, M. M.; Bork, P.; Gottig, S.; Typas, A. Species-Specific Activity of Antibacterial Drug Combinations. *Nature* **2018**, *559* (7713), 259–263.
- (39) Fabio, G. B.; Martin, B. A.; Dalmolin, L. F.; Lopez, R. F. V. Antimicrobial Photodynamic Therapy and the Advances Impacted by the Association with Nanoparticles. *J. Drug Deliv. Sci. Tec.* **2023**, *80*, 104147.
- (40) Lv, X.; Wang, L.; Mei, A.; Xu, Y.; Ruan, X.; Wang, W.; Shao, J.; Yang, D.; Dong, X. Recent Nanotechnologies to Overcome the Bacterial Biofilm Matrix Barriers. *Small* **2023**, *19* (6), No. e2206220.
- (41) Birk, S. E.; Boisen, A.; Nielsen, L. H. Polymeric Nano- and Microparticulate Drug Delivery Systems for Treatment of Biofilms. *Adv. Drug Delivery Rev.* **2021**, *174*, 30–52.
- (42) Heydorn, A.; Nielsen, A. T.; Hentzer, M.; Sternberg, C.; Givskov, M.; Ersbøll, B. K.; Molin, S. Quantification of Biofilm Structures by the Novel Computer Program COMSTAT. *Microbiology* **2000**, *146* (10), 2395–2407.
- (43) Vorregaard, M. Comstat2-a Modern 3D Image Analysis Environment for Biofilms. Technical University of Denmark, DTU, DK-2800 Kgs. Lyngby, Denmark, 2008.
- (44) Kang, X.; Bu, F.; Feng, W.; Liu, F.; Yang, X.; Li, H.; Yu, Y.; Li, G.; Xiao, H.; Wang, X. Dual-Cascade Responsive Nanoparticles Enhance Pancreatic Cancer Therapy by Eliminating Tumor-Resident Intracellular Bacteria. *Adv. Mater.* **2022**, *34* (49), No. e2206765.
- (45) Wang, Y.; Jiang, Y.; Wei, D.; Singh, P.; Yu, Y.; Lee, T.; Zhang, L.; Mandl, H. K.; Piotrowski-Daspiet, A. S.; Chen, X.; Li, F.; Li, X.; Cheng, Y.; Josowitz, A.; Yang, F.; Zhao, Y.; Wang, F.; Zhao, Z.; Huttner, A.; Bindra, R. S.; Xiao, H.; Mark Saltzman, W. Nanoparticle-Mediated Convection-Enhanced Delivery of a DNA Interpolator to Gliomas Circumvents Temozolomide Resistance. *Nat. Biomed. Eng.* **2021**, *5* (9), 1048–1058.
- (46) Huang, P.; Wang, D.; Su, Y.; Huang, W.; Zhou, Y.; Cui, D.; Zhu, X.; Yan, D. Combination of Small Molecule Prodrug and Nanodrug Delivery: Amphiphilic Drug–Drug Conjugate for Cancer Therapy. *J. Am. Chem. Soc.* **2014**, *136* (33), 11748–11756.
- (47) She, W.; Luo, K.; Zhang, C.; Wang, G.; Geng, Y.; Li, L.; He, B.; Gu, Z. The potential of self-assembled, pH-responsive nanoparticles of mPEGylated peptide dendron–doxorubicin conjugates for cancer therapy. *Biomaterials* **2013**, *34* (5), 1613–1623.
- (48) Pei, P.; Chen, L.; Fan, R.; Zhou, X.-R.; Feng, S.; Liu, H.; Guo, Q.; Yin, H.; Zhang, Q.; Sun, F.; Peng, L.; Wei, P.; He, C.; Qiao, R.; Wang, Z.; Luo, S.-Z. Computer-Aided Design of Lasso-like Self-Assembling Anticancer Peptides with Multiple Functions for Targeted Self-Delivery and Cancer Treatments. *ACS Nano* **2022**, *16* (9), 13783–13799.
- (49) Zhao, X.; Zhao, H.; Wang, S.; Fan, Z.; Ma, Y.; Yin, Y.; Wang, W.; Xi, R.; Meng, M. A Tumor-Targeting Near-Infrared Heptamethine Cyanine Photosensitizer with Twisted Molecular Structure for Enhanced Imaging-Guided Cancer Phototherapy. *J. Am. Chem. Soc.* **2021**, *143* (49), 20828–20836.
- (50) Yuan, Z.; Lin, C.; He, Y.; Tao, B.; Chen, M.; Zhang, J.; Liu, P.; Cai, K. Near-Infrared Light-Triggered Nitric-Oxide-Enhanced Photodynamic Therapy and Low-Temperature Photothermal Therapy for Biofilm Elimination. *ACS Nano* **2020**, *14* (3), 3546–3562.
- (51) Yu, J.; Xiao, H.; Yang, Z.; Qiao, C.; Zhou, B.; Jia, Q.; Wang, Z.; Wang, X.; Zhang, R.; Yang, Y.; Wang, Z.; Li, J. A Potent Strategy of Combinational Blow Toward Enhanced Cancer Chemo-Photodynamic Therapy via Sustainable GSH Elimination. *Small* **2022**, *18* (9), 2106100.
- (52) Li, J.; Yi, W.; Luo, Y.; Yang, K.; He, L.; Xu, C.; Deng, L.; He, D. GSH-depleting and H₂O₂-Self-Supplying Hybrid Nanozymes for Intensive Catalytic Antibacterial Therapy by Photothermal-Augmented Co-Catalysis. *Acta Biomater.* **2023**, *155*, 588–600.
- (53) Wei, D.; Yu, Y.; Zhang, X.; Wang, Y.; Chen, H.; Zhao, Y.; Wang, F.; Rong, G.; Wang, W.; Kang, X.; Cai, J.; Wang, Z.; Yin, J.-Y.; Hanif, M.; Sun, Y.; Zha, G.; Li, L.; Nie, G.; Xiao, H. Breaking the Intracellular Redox Balance with Diselenium Nanoparticles for Maximizing Chemotherapy Efficacy on Patient-Derived Xenograft Models. *ACS Nano* **2020**, *14* (12), 16984–16996.
- (54) Odds, F. C. Synergy, antagonism, and what the checkerboard puts between them. *J. Antimicrob. Chemother.* **2003**, *52* (1), 1.
- (55) Hu, D.; Deng, Y.; Jia, F.; Jin, Q.; Ji, J. Surface Charge Switchable Supramolecular Nanocarriers for Nitric Oxide Synergistic Photodynamic Eradication of Biofilms. *ACS Nano* **2020**, *14* (1), 347–359.
- (56) Hussain, S.; Joo, J.; Kang, J.; Kim, B.; Braun, G. B.; She, Z.-G.; Kim, D.; Mann, A. P.; Mölder, T.; Teesalu, T.; Carnazza, S.; Guglielmino, S.; Sailor, M. J.; Ruoslahti, E. Antibiotic-Loaded Nanoparticles Targeted to the Site of Infection Enhance Antibacterial Efficacy. *Nat. Biomed. Eng.* **2018**, *2* (2), 95–103.
- (57) Yuan, Z.; Lin, C.; Dai, L.; He, Y.; Hu, J.; Xu, K.; Tao, B.; Liu, P.; Cai, K. Near-Infrared Light-Activatable Dual-Action Nanoparticle

Combats the Established Biofilms of Methicillin-Resistant *Staphylococcus aureus* and Its Accompanying Inflammation. *Small* **2021**, *17* (13), No. e2007522.

(58) Chen, H.; Cheng, J.; Cai, X.; Han, J.; Chen, X.; You, L.; Xiong, C.; Wang, S. pH-Switchable Antimicrobial Supramolecular Hydrogels for Synergistically Eliminating Biofilm and Promoting Wound Healing. *ACS Appl. Mater. Interfaces* **2022**, *14* (16), 18120–18132.